

# Identifying and understanding strong vibronic interaction effects observed in the asymmetry of chiral molecule photoelectron angular distributions

Gustavo A. Garcia<sup>a</sup>, Héloïse Dossmann<sup>a,†</sup>, Laurent Nahon<sup>a</sup>, Steven Daly<sup>b,‡</sup> and Ivan Powis<sup>b,\*</sup>

<sup>a</sup> *Synchrotron SOLEIL, L'Orme des Merisiers, St. Aubin BP 48, 91192 Gif sur Yvette, France*

<sup>b</sup> *School of Chemistry, University of Nottingham, Nottingham NG7 2RD, UK*

\* Corresponding author ([ivan.powis@nottingham.ac.uk](mailto:ivan.powis@nottingham.ac.uk))

† Current address: Sorbonne Universités, UPMC Univ Paris 06, CNRS, Institut Parisien de Chimie Moléculaire (IPCM), 4 Place Jussieu 75252 Paris Cedex 05 France

‡ Current address: Institut Lumière Matière, UMR5306, CNRS, Université Lyon 1, 69622 Villeurbanne, France

## Abstract

Electron-ion coincidence imaging is used to study chiral asymmetry in the angular distribution of electrons emitted from randomly-oriented enantiomers of two molecules, methyloxirane and trifluoromethyloxirane, upon ionization by circularly polarized VUV synchrotron radiation. Vibrationally-resolved photoelectron circular dichroism (PECD) measurements of the outermost orbital ionization reveal unanticipated large fluctuations in the magnitude of the forward-backward electron scattering asymmetry, including even a complete reversal of direction. Identification and assignment of the vibrational excitations is supported by Franck-Condon simulations of the photoelectron spectra. A previously proposed quasi-diatomic model for PECD is developed and extended to treat polyatomic systems. The parametric dependence of the electronic dipole matrix elements on nuclear geometry is evaluated in the adiabatic approximation, and provokes vibrational level dependent shifts in amplitude and phase, to which the chiral photoelectron angular distributions are especially sensitive. It is shown that single quantum excitation of those vibrational modes which experience only a relatively small displacement of the ion equilibrium geometry along the normal coordinate, and which are then only weakly excited in the Franck-Condon limit, can be accompanied by big shifts in scattering phase; hence the observed big fluctuations in PECD asymmetry for such modes.

## Introduction

The technique of photoelectron circular dichroism[1] (PECD) observes a forward-backward asymmetry in the lab-frame angular distribution of photoelectrons emitted from randomly oriented chiral molecules upon ionization by a beam of circularly polarized light. These asymmetries reverse direction upon exchanging either the molecular enantiomer or helicity of the light and typically range from 1% —40%. Such huge asymmetry factors exceed those of more traditional molecular chiroptical probes by perhaps three orders of magnitude, with a corresponding increase in sensitivity. Being photoionization based, PECD provides a universal approach, requiring no chromophore, and provides orbital specific probing. Because of highly structured energy

dependencies in the chiral distributions, PECD spectroscopy is information rich and naturally adapted to investigation in dilute environments.

Complementing its innate chiral sensitivity, PECD has also proven in detail to be strongly sensitive to both electronic and static nuclear structures (isomerism, conformation, substitution, clustering),[2] and these results can generally be quantitatively reproduced or predicted by calculations made at fixed, equilibrium molecular geometry. This level of approximation is quite common in calculating photoelectron angular distributions generally, and is partly justified by Franck-Condon (FC) assumptions of fully decoupled electronic and vibrational motion.

Of course, non-FC behaviour in photoionization has received much attention, but mainly focussed upon breakdown of vibrational symmetry selection rules, variation of FC predicted branching ratios (cross-sections), and effects of resonances in the photoionization continuum.[3-5] Less common have been theoretically backed investigations of explicit vibrational influences exerted on the photoelectron angular distributions (PADs). The influence of full Herzberg-Teller type vibronic interaction has been discussed[6] in this context, but more typically approaches based upon treating the parametric dependence of the electronic matrix element upon nuclear geometry have provided understanding. Such investigations have mainly addressed the localized K-edge ionization of diatomic[7-11] and triatomic[12, 13] molecules in the vicinity of shape resonances. Only very recently have such case studies extended to consider PADs in larger non-linear polyatomics[14] and/or valence shell ionization.[11, 15] There remains, in any case, little evidence to indicate notable vibrational influence on molecular PADs in regions removed from continuum resonances, other than a near threshold, K-edge study of fixed-in-space CO.[16, 17]

Set against this background, a suggestion of a vibrational dependency in the non-resonant outer valence electron PAD of methyloxirane[18] was interesting and stimulated a further PECD investigation.[19] This latter study provided the unexpected and surprising result that excitation of a specific vibrational mode could provoke a complete reversal in the PAD forward-backward emission asymmetry (switching from -6% to +6%) near to threshold. Furthermore, this reversal appeared to be part of a wider pattern of similarly unexpected, large magnitude variations in the chiral PAD parameters associated with other vibrational modes that could be observed at a higher photon energy.[19] A principal aim for the present paper will be to explore and better understand the wider scope for such enhanced vibrational sensitivity in PECD particularly, and in photoionization PADs more generally. Pragmatically, this will address the question of the extent to which calculations made at fixed equilibrium geometries can be relied upon to help interpret experiments where there is underlying, but perhaps unresolved, vibrational structure.

There is another reason why such investigation may be timely. Very recent work[20-22] has extended the scope of PECD experiments by utilising ultrafast laser-based excitation schemes in place of the established synchrotron radiation sources. Such developments are now attracting considerable interest because of the possibilities for time-resolved chiral probing, and convenient lab-based analytical applications that are thereby opened up.[23-25] In particular, the use of resonantly enhanced multiphoton ionization (REMPI), as opposed to single VUV photon ionization, creates new opportunities for increased vibrational selectivity in PECD, as ionization then occurs out of a prepared vibrational level or wavepacket. [26] Besides permitting greater control of vibrational excitation and mode specificity, REMPI brings with it opportunities for selective isomer and/or

conformer specific ionization.[27] Nevertheless, as this work shows, there are then increased challenges for reliable interpretation in these circumstances.

In the following sections we extend our preliminary work[19] on vibrational PECD in methyloxirane (MOX). As a prototypical chiral molecule, methyloxirane's PECD has been investigated, without vibrational resolution, in both single photon VUV[28-31] and (3+1) REMPI[32] ionization schemes. We have also previously made a comparative study[31] with the analogous trifluoromethyloxirane (TFMOX) and now we continue this to examine at higher resolution the vibrationally-resolved PECD of both molecules. A pseudo-diatomic model has previously been proposed to rationalise the observed PAD asymmetry switching by considering the dipole amplitudes and phases contributing to the PECD phenomenon.[33] This is now developed and extended to provide a more realistic polyatomic model and a first application is made to specific vibrational modes in the present experimental observations.

## Methods

### Experimental methods

Experiments were performed at the SOLEIL synchrotron facility using the vacuum ultraviolet (VUV) variable-polarization undulator-based beamline DESIRS.[34] The high flux, moderate resolution 200 gr/mm grating was chosen and a gas filter,[35] filled with 0.25 mbar Ar, removes any high order undulator harmonics passing the monochromator. The degree of circular polarization was determined and checked by measurements made with a dedicated in situ VUV polarimeter.[36]

Enantiomerically pure commercial samples of TFMOX (Tyger Scientific Inc. for S-TFMOX and Aldrich for R-TFMOX) and MOX (Aldrich) were directly poured into a cooled double-walled bubbler refrigerated at -15 °C and -17 °C, respectively. The resulting vapor was mixed with 0.5 bars of He and expanded through a 50 μm nozzle. The seeded supersonic beam passed through a 0.7 mm (TFMOx) or 1.0 mm (MOx) skimmer to reach the ionization chamber where it crossed the photon beam at a right angle in the center of the DELICIOUS II spectrometer.[37] Emitted electrons are then accelerated into a velocity map imaging (VMI) electron spectrometer, while the corresponding ions are detected in coincidence with a linear Wiley-McLaren time-of-flight analyzer. The coincidence scheme allows impurities and background to be filtered out by only considering photoelectrons correlated to the MOX or TFMOX cations.[31]

### Threshold electron spectra

For the photon energy-scanned spectra the monochromator slits were set to provide a photon resolution of 3-5 meV and all the data were corrected by the photon flux, as measured with a photodiode (AXUV, IRD Inc.) located right after the interaction region. In the case of MOX, the 4s and 4s' absorption lines of Ar provided the absolute energy scale, while for TFMOX, the  $H^3\Pi_u \leftarrow X^3\Sigma_g^-$  absorption lines of O<sub>2</sub> were used. The recorded photoionization matrices providing the electron intensity as a function of both photon and electron kinetic energy, were treated following the procedure described elsewhere[38], accepting electrons having ≤100 meV energy to obtain a slow photoelectron spectrum (SPES), with an estimated 10 meV overall resolution.

### Photoelectron Circular Dichroism

PECD measures a forward-backward asymmetry in the photoelectron angular distribution from a randomly oriented sample. The general normalized form of the PAD, in the case of one-photon ionization, is:

$$I^{(p)}(\theta) = 1 + b_1^{(p)} P_1(\cos \theta) + b_2^{(p)} P_2(\cos \theta), \quad \text{Eq. 1}$$

where  $\theta$  is the angle measured from the light propagation direction and the  $P_j$  are Legendre polynomials. Of interest for PECD is the chiral  $b_1$  parameter, which is only non-zero for chiral target molecules ionized with left ( $p=1$ ) or right ( $p=-1$ ) circularly polarized light (respectively LCP and RCP) and hence perfectly encapsulates the chiral response. The sign of  $b_1$  changes with polarization,  $p$ , or with exchange of a molecular enantiomer, whereas  $b_2$  is invariant. Consequently, forming the difference, or dichroism LCP-RCP, of the photoelectron angular distribution can isolate the chiral parameter:

$$I^{(+1)}(\theta) - I^{(-1)}(\theta) = (b_1^{(+1)} - b_1^{(-1)}) P_1(\cos \theta) = 2b_1^{(+1)} \cos \theta, \quad \text{Eq. 2}$$

where the Legendre polynomial term has been expanded out in the last step. This operation also helps cancel any residual instrumental asymmetry in the angular distribution, such as imaging detector gain inhomogeneity, which does not vary with the polarization state.[39]

For recording PECD the spectrometer extraction fields were set high enough to collect all the electrons onto the detector, and the monochromator slits were adjusted only to control the photon flux (count rate). For each selected photon energy, and for a given enantiomer, several mass-selected photoelectron images were acquired alternating left and right circularly polarized light (LCP and RCP). The images were then combined following a previously defined methodology[39] to obtain the total LCP+RCP and the difference LCP-RCP, from which the photoelectron spectrum and PECD ( $b_1$ ) can be respectively extracted after Abel inversion.[40] The PECD data were corrected by the amount of circular polarization as defined by the Stokes parameter  $S_3$ , which was precisely determined at the time of the measurement and found to be in the interval 0.95–0.99 across the whole photon energy range employed. Experimental error bars are calculated applying standard error propagation formulae assuming an initial Poisson distribution on the pixel intensities of the VMI images.

### Computational

Harmonic oscillator vibrational analyses for the neutral and ground electronic state cation were performed using the Gaussian09 program.[41] For MOX, B3LYP/cc-pVTZ calculated frequencies were obtained and subsequently used with a scaling factor of 0.97 applied.[42, 43] For TFMOX, such density functional calculations failed to provide a basis for realistic looking Franck-Condon simulations, for reasons that are unclear. Consequently MP2/6-311++G(d) calculated vibrational modes were employed for this molecule, with a frequency scaling factor of 0.95. Franck-Condon factors, and vibrational PES simulations were prepared from these normal mode analyses using both Gaussian09[41] and FC-Lab II software.[44]

Electric dipole matrix elements for the photoionization were calculated at fixed geometry using the continuum multiple scattering method with a Slater  $X\alpha$  exchange-correlation potential (CMS- $X\alpha$ ). Precise details are as provided in our previous publication on these molecules.[31] Photoionization cross-sections and angular distribution parameters for fixed equilibrium geometries are obtained from these, again as described previously.[1, 45, 46] The calculation of vibrational mode-specific PAD parameters will be discussed further below.

## Results and Discussion

### Methyl Oxirane

Figure 1 presents a high resolution ( $\sim 10$  meV) photoelectron spectrum of the HOMO band of MOX. Compared to an earlier threshold electron spectrum[19] this SPES achieves a lowered background due to the improved treatment of “hot” electrons in the SPES method.[38] Because of the reliable calibration against Ar atomic absorption lines, we have also revised the adiabatic ionization energy (IE) down by 10 meV to  $10.24 \pm 0.01$  eV. Nevertheless, it is notable that the weak, labelled features are visible in both the threshold and SPES spectra, and so are quite reproducible. Also included in Fig. 1 is a Franck-Condon simulation of the spectrum, calculated with an assumed FWHM similarly of  $\sim 10$  meV. For clarity only the most intense calculated transitions are plotted in the underlying stick spectrum and are labelled with lower case letters for single quantum excitation and upper case letters for vibrational combinations/composite excitations. In broad overview, the HOMO band displays three or four prominent peaks, which from the simulation we can assign (although not uniquely) as a progression of increasing quanta of modes  $\nu_{10}$ ,  $\nu_{11}$ , and combinations thereof. However, in between one sees weaker transitions involving first single quanta, then combinations, of lower frequency deformation modes,  $\nu_2 - \nu_5$ .

Vibrationally-resolved PECD of S-MOX has been recorded at four additional photon energies, and with our previous  $h\nu = 10.4$  eV, 10.7 eV measurements[19] now gives a measurement set that spans

the range  $h\nu = 10.4 \text{ eV} - 11.5 \text{ eV}$ . All VMI image data sets have been reanalysed to extract the PECD, which we here present as  $b_1^{\{+1\}}$  PAD parameters. As a check the 11.5 eV measurement was also replicated using the R-MOX enantiomer; apart from the anticipated sign change with enantiomer switch the PECD result was effectively identical, demonstrating good reproducibility.

The  $h\nu = 10.4 \text{ eV}$  result is shown in Fig. 2 with the PES and vibrational assignment indicated on a common energy scale. Most striking is the previously reported reversal of the PAD asymmetry ( $b_1^{\{+1\}} : -0.03 \rightarrow +0.03$ ) between the features  $c$  and  $D$ . But it is also possible to infer that each of the vibrational features  $a, b, c, D$  has associated with it a different value of the PECD. The VMI PES in this figure is nearly superimposable on the SPES, indicating similar resolution. The VMI technique, however, provides a constant resolving power so that as photon energies (and corresponding electron energies) are increased, and the extraction fields adjusted to keep a full detector image, the *absolute* resolution achieved will degrade.

This lowered resolution can be observed in Fig. 3 which shows the  $h\nu = 10.8 \text{ eV}$  data. The very weak feature  $b$  can no longer be discerned in the VMI PES or PECD. Nevertheless, the PECD curve from threshold to 10.8 eV closely resembles that recorded at  $h\nu = 10.4 \text{ eV}$ , albeit consistently shifted by  $\sim 0.07$  to more negative  $b_1$ . This shift in the aggregate (or overall) PECD is just the variation with increasing electron kinetic energy that was previously observed in the near threshold, but vibrationally un-resolved, HOMO electron PECD study.[31] Nevertheless, in detail now there is clearly further structure with non-monotonic variations of the  $b_1$  value that correlate with vibrational features across the ionization energy range under observation. In particular, there is again a big jump of  $\sim 0.6$  on progressing from  $c$  to  $D$ . The trends from our complete MOX data set are summarised in Fig. 4. Here we have extracted the  $b_1$  values at each peak, by fitting Gaussian functions to the VMI PES with centres fixed by the calculated peak positions, and then using these to form weighted mean values. This falls short of a full deconvolution, which is precluded by the high density of vibrational states, and the values obtained will be to some extent blended, especially at higher energy as the resolution degrades. In the top panel of Fig. 4 one compares the PECD for the prominent peaks  $a, E, H$  and two of the intermediate peaks,  $c$ , and  $D$  at successive photon energies. At any given photon energy, the vibrational level dependent  $b_1$  values shift systematically more positive as vibrational frequency increases  $a \rightarrow H$ , with the clear exception of  $c$  ( $4^1$ ), which is always the most negative.

The PECD,  $b_1$ , can be expected to vary with electron kinetic energy (momentum). One has hence to consider whether an apparent correlation with vibrational features is no more than such an energy dependence, the electron energy at each photon setting being anti-correlated with vibrational energy. The lower panel in Fig. 4 therefore replots the same data, but now as a function of electron energy. It is seen that, certainly at lower energies, nearly all the peaks fall on the same trendline. This therefore suggests that the variations are indeed electron energy, rather than vibrational mode, related. The one clear exception to this common trend across the full range studied is the feature  $c$  ( $4^1$ ).

Although for clarity peak  $F$  has been excluded from Fig. 4, it deserves further comment. As seen in Fig. 1 the two transitions to the high energy side of this composite feature are assigned as combinations involving single quantum of  $\nu_4$ . In Fig 3 one can see a dip in the rising trend of  $b_1$ , just as observed for the pure  $4^1$  excitation, and this is quite generally true (see for example the  $h\nu = 10.7$

eV data set in Fig. 4 of Ref. [[19]] ). Overall, there are very strong indications that the  $\nu_4$  mode is somehow anomalous, both when excited individually and possibly also when in combination with another mode. In all cases, this behaviour clearly suggests via the vibrational dependence of the chiral asymmetry at each given electron kinetic energy breakdown of the full FC approximation, meaning that the electron continuum and nuclear motion are not decoupled.

Some hints, or at least a rationalization of why this may be come from examining the nature of the vibration (see animations provided in Supporting Information). Mode  $\nu_4$  is an asymmetric deformation of the epoxy ring, essentially a stretching of the O-C(2) bond. The HOMO orbital of MOX is a  $2p$  lone pair localized on the oxygen atom, while C(2) is the asymmetrically substituted carbon. In other words the separation of the initial orbital from the stereogenic centre of MOX is strongly modulated by this particular vibration. One may suppose that this in turn impacts the scattering of the outgoing electron by the chiral centre, by virtue of which it senses the molecular handedness and generates in response a forward/backward asymmetry in the electron emission. Contrast this with the more prominent (and near degenerate)  $\nu_{10}$ , and  $\nu_{11}$  modes which are effectively CH wagging motions, leaving the epoxy ring, and specifically the O-C(2) separation, unaffected.

### Trifluoromethyloxirane

The trifluoromethyloxirane threshold electron spectrum (scanned photon energy) was previously[31] reported upon, with the adiabatic ionization energy determined against the photon energy calibration as  $11.195 \pm 0.007$  eV. For this work PECD measurements were made at selected photon energies ranging up to 11.8 eV. The energy scales for these VMI PES and PECD spectra have in turn been calibrated against the threshold spectrum.

In Fig. 5 we show the lowest energy  $h\nu = 11.35$  eV spectrum, approximately 155 meV above threshold, and so analogous to the Fig. 2 MOX measurement. Remarkably, the TFMOX PECD again shows a dramatic reversal in the forward-backward photoelectron asymmetry. The  $S$ - enantiomer  $b_1$  parameter switches from -0.03 to +0.03 in a region falling between distinct major peaks in the PES, before returning negative. The FC simulated spectrum indicates some very weak vibrational transitions in this region, with correlated structure evident in the PECD that can be assigned successively to modes  $\nu_2$ ,  $\nu_8$ ,  $\nu_{10}$ , and  $\nu_{11}$ . Then, as excitation reaches to the  $\nu_{12}$  region,  $b_1$  flips negative again while approaching the strong  $\nu_{15}/\nu_{16}$  excitation. We comment that a general advantage of PECD has been shown in its ability to reveal underlying orbital electronic structure even in spectrally congested regions where individual orbitals are not resolved in the PES. [39, 47-49] This arises because there may often be large variations in  $b_1$  (in magnitude and sign) between adjacent orbitals even while the cross sections are quite commensurate — with consequently little distinguishable variation in intensity of the regular spectrum. In a somewhat similar manner, PECD may here provide clues to the position of vibrational transitions, even when these are too weak and the resolution insufficient, to show as significant structure in the PES alone. With this in mind we note that modes  $\nu_2$ ,  $\nu_8$  are clearly discernible in the PECD of TFMOX of TFMOX (Fig.5) although not in the PES, and similarly modes  $\nu_4, \nu_5$  are much more strongly delineated in the MOX PECD (Fig.2) than its PES.

A further TFMOX VMI PES measurement recorded at  $h\nu=11.8$  eV appears in Fig. 6 along with the full simulated HOMO PES band. The overall agreement with the simulation is excellent. It may be noted that VMI energy resolution degrades moving outwards across an image, so that the apparent

reduction in experimental resolution of the finer predicted structure at the lower ionization energies is expected. The coarse structure of the HOMO PES consists of four prominent peaks,[31] and from the simulation this can be assigned as dominantly a progression in  $\nu_{15}$ . However, it is clear that there is in fact a repeating pattern of single quantum excitation of modes  $\nu_2, \nu_8, \nu_{11}, \nu_{12}, \nu_{16}$  (see animations in Supplementary Information) in combination with 0–3 quanta of  $\nu_{15}$  contributing to each coarse feature. Under favourable conditions, this gives rise to resolvable sub-structure. If then one extends this comparison of predicted vibrational excitation to the PECD spectrum included in Fig. 6 a somewhat similar repeating pattern emerges. The PECD displays maxima corresponding exactly with each of the  $\nu_{15}$  major PES peaks, with valleys in between; in more detail one can tentatively identify shoulders at transitions  $15^x2^1$ , a minimum at  $15^x8^1$ , a partial increase and possible oscillation in the vicinity of  $(15^x11^1, 15^x12^1)$ , followed finally by a sharp rise to the next peak at  $(15^{x+1}, 15^x16^1)$ , where  $x$  represents the number of quanta,  $x=0\dots2$ . This repeating vibrational excitation pattern suggests that having a single quantum in cation modes  $\nu_2, \nu_8, \nu_{11}$ , or  $\nu_{12}$  reduces the magnitude of the PECD relative to an unperturbed value observed at the major  $\nu_{15}$  ( $\nu_{16}$ ) peak positions.

An overview of all TFMOX PECD recordings, made with both R- and S- enantiomers and overplotted on the same ionization energy scale, is presented in Fig 7. Following theoretical expectations that the two enantiomers' PECD differ only in sign, the S- enantiomer data is negated for plotting, facilitating visual comparisons. First, it is evident that individual curves are successively displaced to more positive  $b_1$  with increasing photon energy (correspondingly with mean kinetic energy) and this is a priori a non-specific consequence of the generalized electron continuum dynamics. Secondly, Fig. 7 clearly confirms a more specific correlation, as just inferred from Figs. 5 and 6, of the PECD structure at each fixed ionization energy with expected vibrational excitations.

Fig. 8, shows the electron kinetic energy dependence of TFMOX  $b_1$  values at selected vibrational peak positions (as identified by the PES Franck-Condon simulation), analogous to the lower panel Fig. 4 drawn for MOX. With the increased number of assignable features in TFMOX, including multiple quanta excitations, some additional insights can emerge. The displacement of the data curves away from a single  $b_1$  vs. KE trendline in Fig. 8 reveals a rich vibrational dependence of the PECD superimposed on the overall positive correlation of the aggregate  $b_1$  with increasing electron energy (as predicted by the equilibrium geometry calculation in this close-to-threshold region). First,  $b_1$  values for the nominal progression in  $\nu_{15}$  ( $15^1, 15^2, 15^3$ ) are the most positive and loosely cluster around the same trend line, distinct from all the other levels examined. Second, excitations involving mode  $\nu_8$  — that is  $8^1, 15^18^1, 15^28^1$  — are closely clustered about a common trendline in this figure. The combination bands  $15^12^1$  and  $15^22^1$  are also distinct and follow their own unique trendline, while common behavior can also be seen in the combinations  $15^111^1$ , and  $15^211^1$ . However, the single quantum excitation of  $\nu_2$  and  $\nu_{11}$  both show more independent behavior, with the curve for the excitation  $11^1$  being the most strongly displaced from those of  $\nu_{15}$ .

Finally, we comment on the data for the origin 0-0 peak. Its Fig. 8 trendline is parallel to, and falls exactly in the middle of, all the other data, but it can be seen that in the individual spectra (Fig. 6 & 7) the  $b_1$  values are not constant but decrease across the PES peak profile. Most likely this is due to more negative values associated with the adjacent  $2^1$  excitation being blended in by the reduced experimental resolution at this end of the spectra. Consequently, one may suppose that a better measure of  $b_1$  for the 0-0 transition could be read from the left edge in Fig. 6 & 7, effectively

displacing the 0-0 trendline in Fig. 8 0.02 units more positive, whence it becomes more closely associated to the  $\nu_{15}$  ( $15^1$ ,  $15^2$ ,  $15^3$ ) grouping. With the benefit of such an adjustment it follows that the most intense peaks observed in the PES, the  $\nu_{15}$  progression built on the origin, also correspond to the maximum PECD decoupled from the generalized, vibrationally non-specific increase with electron kinetic energy.

However, it should be noted that the vibrational assignments labeled in Fig. 8, and used in the discussion, reflect the dominant contribution to an observable PES peak identified by the Franck-Condon simulation. For example, the near degenerate  $\nu_{16}$  and  $\nu_{15}$  levels cannot be experimentally distinguished and so the experimental “ $\nu_{15}$ ” peaks will in fact all be a composite of both modes. For other nominal levels finite experimental resolution will also lead to some blending with adjacent values. Deconvolution of PECD for transitions involving modes  $\nu_{11}$  and  $\nu_{12}$  proved difficult so again these levels are not properly distinguished.

Notwithstanding such difficulties, earlier qualitative inferences drawn from our discussion of Fig. 6 seem to be more quantitatively corroborated and extended: PECD asymmetry is maximised for excitation of an arbitrary number of quanta of the strong mode  $\nu_{15}$  (and implicitly  $\nu_{16}$ ), but excitation of a single quantum of other modes, in combination with  $\nu_{15}$  or alone, is sufficient to perturb or reduce the PECD asymmetry. Specifically, for  $\nu_2$  and  $\nu_8$  the observed PECD appears to be uniquely determined by the presence in combinations of a single quantum of these modes in the final cation state, while the single quantum  $\nu_{11}$ / $\nu_{12}$  excitation produces the biggest divergence.

### Theoretical Model

One of the authors recently proposed[33] a rationalization for the unexpected vibrational sensitivity of PECD observed in our preliminary MOX results.[19] This used a pseudo-diatomic model based upon the transiently chiral hydrogen peroxide, but treating the displacement of the ion equilibrium geometry as an adjustable parameter. Because of its strong influence upon the scattering phase of the photoelectron, this parametrized displacement was shown to be decisive in promoting the kind of asymmetry reversals experimentally observed when a single vibrational quantum was weakly excited.[33]

Here we wish to develop and extend that model to afford a polyatomic treatment using a fully realistic set of vibrational parameters on an experimentally feasible chiral system. Starting from a normal mode harmonic analysis, which we remark is the basis for successfully simulating the threshold electron spectra, the displacement of the ion potential (equilibrium geometry) is expressed in normal mode coordinates (see Supplementary Information). A single active mode is then selected, all others being frozen, and the photoionization dynamics are evaluated allowing for motion along that coordinate and the projection of the vibrational wavefunction from neutral to ion potential. Implicit in this treatment is an assumption of a unique 1:1 mapping of neutral and ionic vibrational modes (parallel approximation), whereas in practice Duschinsky rotation may cause mode mixing. In Fig. 9 we show the Duschinsky matrices for MOX and TFMOX calculated for the vibrational simulations in, respectively, Figs 1 and 6. Both show evidence for mode mixing in the ionization, but that for TFMOX is nearer the ideal diagonal form, especially for the lower frequency modes that are of particular interest here. In particular in the MOX cation  $\nu_4$ , which has been identified to be of especial interest, is unfortunately very heavily coupled to other modes by the Duschinsky rotation. Consequently, we henceforth focus on the TFMOX modelling, although here

too there is Duschinsky mixing affecting e.g. modes  $\nu_{11}$ ,  $\nu_{15}$ . To apply a treatment for coupling of electronic and nuclear degrees of freedom in the parallel mode approximation we hence use the Duschinsky matrix to identify the single dominant mappings  $\nu'' \rightarrow \nu'$

Using the Born-Oppenheimer approximation (adiabatic limit) the matrix elements for photoionization,  $T$ , can be written separated into a purely electronic,  $E$ , part which may nevertheless have a parametric dependence upon  $Q$ , the vibration coordinate.

$$T_{i,v,f,v',\bar{k},\hat{\eta}} = \left\langle \chi_{i,v}(Q) \left| E_{i,f,\bar{k},\hat{\eta}}(Q) \right| \chi_{f,v'}^+(Q) \right\rangle_Q, \quad \text{Eq. 3}$$

$$E_{i,f,\bar{k},\hat{\eta}}(Q) = \left\langle \varphi_i(r;Q) \left| \hat{\varepsilon}_{\hat{\eta}} \right| \varphi_{f,\bar{k}}^{(-)}(r;Q) \right\rangle_r,$$

where  $i$  and  $f$  denote respectively the initial (neutral) and final (ion + electron) states, the  $\chi(Q)$  are vibrational wavefunctions, and the  $\phi(r;Q)$  are appropriately normalised electronic functions;  $\hat{\varepsilon}_{\hat{\eta}}$  is the dipole operator. Quantitative treatments, averaging the electronic matrix elements over the vibrational motion along  $Q$  as implied by Eq. 3, have been successfully applied by a number of previous authors[5, 7-9, 12, 17] to explain Franck-Condon breakdown in linear molecules and is at the core of our PECD treatment.[33] Calculation of the pure electronic matrix elements,  $E_{i,f,\bar{k},\hat{\eta}}(Q)$ , prior to such  $Q$  averaging is here performed using the CMS-X $\alpha$  method, as previously described.[31]

Fig. 10(A) shows how the PECD, calculated from electronic matrix elements at the fixed equilibrium molecular geometry,[1, 45] provides excellent agreement with experimental HOMO electron data points obtained by forming intensity weighted PECD averages taken over the PES HOMO band profile.[31] Given the great variation of PECD with vibrational level revealed above, it might be somewhat surprising that a fixed geometry calculation, completely ignoring vibrational motion, can perform so well against vibrational averaged (unresolved) experimental data, a point to which we return later, in Conclusions.

In Fig. 10(B), we also show a number of PECD calculations where the matrix elements have first been sampled over the coordinate space of selected modes in the neutral ground state using  $(\chi_{i,0}(Q))^2$  as a weighting function. The zero point motion in the respective modes is thereby partially acknowledged, while the excited state vibrational details have yet to be included. The results for modes  $\nu_2$  and  $\nu_{15}$  barely differ from the fixed equilibrium geometry calculation in Fig. 10(A), although bigger deviations are observed for modes  $\nu_8$ ,  $\nu_{11}$ ,  $\nu_{12}$ . Nevertheless, it does not appear that sampling the zero point motion in this manner is alone sufficient to explain the experimental findings. On the other hand, ignoring zero point vibrational motion by the proposed freezing of all but the selected active mode is a necessary simplification at this stage. One may speculate, however, that for those modes that do deviate from the norm as a consequence of such allowance for zero point motion, there may overall be some fortuitous mutual cancellation. This in turn may justify the apparent success in Fig 10 (A) of a fixed equilibrium geometry calculation reproducing the vibrationally unresolved experimental PECD.

In Fig 11 we show the results for selected modes obtained by calculating the PECD after a full averaging of the electronic matrix elements over the vibrational motion as expressed in Eq. 3. The numerical scheme to implement this follows a previous description.[33] In effect the vibrational

coordinate is sampled with a  $\chi_{i,v}(Q) \chi_{f,v'}^+(Q')$  weighting function, assuming a 1:1 mapping of normal coordinates between neutral and ion. This weighting function thus incorporates the ion and neutral vibrational parameters, but also depends upon the relative displacement  $Q \rightarrow Q'$ . Photoionization cross-sections calculated from this vibrational specific model (i.e. without the FC approximation) appear as insets in Fig. 11. Those modes ( $\nu_2, \nu_8, \nu_{11}, \nu_{12}$ ) appearing with only single quantum excitations in the FC simulations, and by implication in the experimental photoelectron spectra, (Figs 5 & 6) have a reduced  $\nu=1:\nu=0$  cross section ratio, and negligible  $\nu=2$  intensity. Mode  $\nu_{15}$ , in contrast, has approximately comparable  $\nu=0, 1, 2$  calculated cross-sections, and correspondingly appears as a strong progression in the FC simulation. Unsurprisingly, these different calculated behaviours correlate with the calculated magnitude of the ion potential displacements along the normal mode coordinate (listed in Supporting Information), as understood in familiar qualitative discussion of the FC Principle.

However, we previously identified[33] that relatively small geometry displacement could also exert a major influence upon the phase of matrix elements averaged as in Eq. 3, specifically for a vibrational excitation  $0 \rightarrow 1$ . For calculation of e.g. vibrational branching ratios this is of little consequence, as cross-sections are not phase dependent. But for PECD, which is strongly phase dependent (more so than traditional angular distribution measurements), this assumes a great importance.[1]

Summarising that previous argument[33] we note that the vibrational averaging in Eq.3 can be re-written as

$$T_{i,v,f,v'} \equiv \int_{-\infty}^0 \chi_{i,v}(Q) \chi_{f,v'}^+(Q) E_{i,f}(Q) dQ + \int_0^{\infty} \chi_{i,v}(Q) \chi_{f,v'}^+(Q) E_{i,f}(Q) dQ \quad \text{Eq. 4}$$

where for simplicity some subscripts have been dropped and the integration, separated into positive and negative domains of  $Q$ , written explicitly. For a small relative displacement, and  $0 \rightarrow 1$  excitation, the weighting function  $\chi_{i,0}(Q) \chi_{f,1}^+$  is approximately antisymmetric about  $Q=0$ . This is illustrated in Fig. 12. If it is further assumed that the electronic matrix elements,  $E$ , vary only slowly with  $Q$ , the half integrals over positive and negative domains may be of similar magnitude, but opposite sign. However, the electronic matrix elements are complex, and multiplication by -1 in effect induces an additional phase shift of  $\pi$ . Viewed in the complex plane, the combination of the integrals over the intervals  $[-\infty, 0]$  and  $[0, \infty]$  can thus be viewed as taking a difference of two commensurate vectors; the resultant magnitude is small (hence a weak cross-section results) but also the phase or direction of the resultant vector can vary widely with even small differences in absolute magnitude, again as illustrated in Fig. 12(D). Since PECD is very sensitive to small phase shifts (in fact to the sine of the phase differences between adjacent partial waves) this combination of circumstances can provoke large variations in the predicted  $b_1$  parameters.

Examining, finally, the vibrational resolved PECD calculations in Fig. 11, one sees that for all modes considered the  $b_1(\nu=0)$  curves barely differ from the fixed equilibrium geometry calculation. Very significant deviations can, however, emerge when the  $\nu=1$  predictions are examined, and especially in the region 0.2 – 1 eV kinetic energy. Qualitatively, the results for  $\nu_{15}$  (lowest panel) look very different from those of the other treated modes. This is the mode with the largest ion geometry displacement and its  $b_1$  shifts to more positive values (by  $\sim 0.02$  units) with each successive added

quantum. This parallels the behaviour of the  $\nu_{15}$  progression as displayed in Fig. 8, although we again caution that the experimental  $\nu_{15}$  values will in fact be composite values incorporating at least  $\nu_{16}$  excitation as well; hence fully quantitative agreement is not sought.

For the less displaced, more weakly excited vibrations, especially modes 2, 8, and 12, the predicted  $b_1$  curves for  $\nu=1$  vary more dramatically, and in the region of most interest from just above threshold there is a consistent shift towards more negative  $b_1$  values. This includes regions very close to threshold where the sign of the predicted  $b_1$  for the  $\nu=1$  levels actually switches to negative values, qualitatively as observed in the  $h\nu = 11.35$  eV spectrum (Fig. 5). Perhaps more significant is the magnitude of the displacement between the  $\nu=0$  and  $\nu=1$  curves, which is typically 0.03 — 0.08  $b_1$  units in the near threshold region. This conforms closely to the general experimental observations (perhaps most easily seen in Fig.8).

Summarising, the predicted PECD sensitivity of those vibrational modes with small geometry displacements (and which are thus only weakly excited in the FC approximation) is in good accord with the experimental observations that have been presented. Conversely, predictions for the strongly displaced, strongly excited  $\nu_{15}$  mode show the opposite — larger asymmetry that increases with successive quanta — again according well with experiment. Although the theoretical model excludes multimode combinations by considering only the excitation of single vibrational modes, with all other modes frozen, the experimental observation of a repeating PECD pattern across successive members of the complex progression in  $\nu_{15}$  further supports a view that excitation of a single quantum of the weak modes may always perturb expectations by its impact on the scattering phase.

## Conclusions

The experimental results presented here demonstrate strikingly how the photoelectron angular distribution, and specifically the chiral asymmetry examined by photoelectron circular dichroism measurements on randomly-oriented targets, is strongly influenced by the excitation of vibrational modes in the cation formation. The two molecules examined, methyloxirane and its trifluoromethyl analogue, are clearly related, yet maintain dissimilarities in their overall photoionization detail[31] and, as seen here, in the detail of the vibrationally induced PECD structure. In methyloxirane the vibration  $\nu_4$  seems especially to modify the PECD, and the nature of the vibrational motion (and the localised HOMO) suggests a simple phenomenological explanation may apply. Yet in trifluoromethyloxirane there are several weakly excited, skeletal deformation type vibrational modes that seem to modulate the PECD, precluding such a simple explanation; indeed the analogous motion to  $\nu_4$  in methyloxirane,  $\nu_9$ , is predicted to be negligibly excited in trifluoromethyloxirane.

Analysis of these experiments starts from Franck-Condon simulations that rather successfully reproduce the vibrational resolved PES HOMO band profile for both molecules, and so provides vibrational assignments. But since electronic and nuclear motions are fully uncoupled in the Franck-Condon approximation, it cannot provide a basis to explain the strong vibrational dependence of chiral terms in photoelectron angular distribution that are observed by PECD. A parameterised quasi-diatomic model calculation, proposed to explain vibronic coupling and its influence on PECD[33] has here been extended and developed to provide a more realistic polyatomic molecule prediction and applied to the trifluoromethyloxirane system. These new calculations retain a simple model where electronic-nuclear modes couple within the adiabatic limit as a consequence of the

geometry dependence of the phase and amplitude of the dipole matrix element. The resulting vibrational cross-sections (which incorporate no phase-dependent interference terms) do not differ significantly from the successful Franck-Condon predictions that ignore all geometry dependence. This underscores a presumption that it is geometry-induced phase shifts in the coordinate averaged matrix elements that vary the interference terms contributing to PECD[33] and so account for the dramatic fluctuations observed. In a similar manner, phase shifts have been ascribed as being responsible for the vibrational dependence on molecule-frame PADs observed on fixed-in-space CO.[16]

The present calculations retain a number of simplifying approximations beyond the adiabatic model. In particular all vibrations but the selected active mode are frozen, their zero point motion ignored, and Duschinsky rotation of the modes is ignored; simultaneous combination excitations of more than one mode are not treated. Moreover, calculating the electronic photoionization matrix elements the near threshold region (<1 eV kinetic energy) is especially challenging. The electron dynamics can be expected to be most sensitive to the molecular potential in this regime, thus placing great demands on the subtleties, but also the absolute attractiveness (ionization energy) of the potential if fully accurate matrix elements are expected. The precision (< 50 meV) and range of the experimental observations falls well inside anticipated uncertainty in the calculated electron energy scale, so that caution is required in making direct point-point comparison of theory and experiment. From an experimental perspective it has been noted that the near degeneracy of e.g.  $\nu_{15}$  and  $\nu_{16}$ , and the effects of finite experimental resolution blending contributions of other levels, means that the vibrational quantum assignments indicated for experimental data points are nominal.

For the foregoing reasons we should not expect to achieve a fully quantitative theory-experiment comparison. Nonetheless, a semi-quantitative reproduction of key features is achieved. Importantly, different behaviour of the weakly excited vibrational modes is correctly predicted to show greatest impact with a single quantum excitation, and to be different in nature to behaviour of the strongly excited modes that dominate the full spectrum. As would be recognised in qualitative undergraduate discussion of the Franck-Condon Principle, the difference corresponds to those modes where the displacement between neutral and ion potentials (along the normal mode coordinate) is, respectively, small or large. In the context of our vibrational PECD model,[33] summarised here, smaller displacements also correlate with much greater variation in resultant phase, and hence an enhanced impact upon the associated PECD.

It may reasonably be asked how, given such great variation of  $b_1$  with vibrational state of the ion, more routine calculations made neglecting vibrational motion at fixed neutral geometry can have the success they undoubtedly do. For example, Fig 10(A) illustrates the good reproduction of vibrational unresolved PECD data by a fixed, equilibrium geometry calculation for the trifluoromethyloxirane molecule. Experimental conditions that either fail, or do not seek, to achieve resolution of the vibrational structure will in effect be averages formed across the relevant PES band profile. Inevitably such mean, unresolved PECD measures will then be dominated by the PECD associated with regions of highest intensity (cross-section) i.e. for trifluoromethyloxirane the PECD maxima of the  $\nu_{15}/\nu_{16}$  progression can be expected to dominate the mean PECD and these prominent progressions have PECD that is well behaved, lying close to the equilibrium geometry calculation. The more aberrant behaviour displayed by those excited modes having small

equilibrium displacement and consequently reduced cross section will contribute only weakly to an averaged mean PES and PECD.

One unanticipated experimental observation is that the divergent PECD asymmetry associated with single quantum excitation that occurs at ionization energies below the prominent  $\nu_{15}/\nu_{16}$  peak in trifluoromethyloxirane, and which is semi-quantitatively replicated in our calculation, similarly recurs when these weak modes are excited in combinations with the strong  $\nu_{15}/\nu_{16}$  progression. There is consequently a repeating pattern that can be discerned in the PECD spectrum in regions between the prominent PES peaks, and that is in turn superimposed on a monotonic, non-vibrational state-specific variation of PECD with electron energy. In detailed examination (Fig. 8) it appears as though the presence of a single quantum excitation of one of these weak, small equilibrium displacement modes uniquely determines the PECD, regardless of the number of  $\nu_{15}$  quanta simultaneously excited. Multimode excitations are not currently incorporated in our model, but the implied extension of our single mode findings looks plausible. The phenomenon rather reinforces our empirical notion of an “unperturbed” PECD, found for strongly excited vibrational modes, versus a “perturbed” PECD associated with small equilibrium displacements of the ion equilibrium geometry (and hence smaller FC-type PES intensities for excited levels). The linkage in these concepts is found in the enhanced phase shifts associated with small equilibrium displacements according to our model.

Currently, opportunity for vibrational resolution in the VUV photoionization of typically sized chiral molecules is rather limited, hence the relative novelty of these current measurements. Of course, one may anticipate that with technical developments in light sources, detectors and analyzers more such measurements will be forthcoming. The recent development of resonance enhanced multiphoton PECD (MP-PECD)[20, 21, 23] will, however, surely bring its own increased opportunities to explore vibrational effects, either directly by exploiting additional sensitivity and selectivity in laser excitation of a resonant intermediate to explore and control vibrational quantum states in the ion, or through the evolution of vibrational wavepackets prepared in time domain PECD measurements. Recent work has showed how selective excitation of specific vibronic bands in resonant ionization could be used to achieve conformer specific ionization in a two-photon absorption CD measurement,[27] something that would be of great interest for MP-PECD. Understanding potential vibronic interactions would, however, be essential for properly interpreting conformer differences in such circumstances. Even when there is no explicit vibrational resolution in large molecule PECD, the possession of a general understanding of how underlying vibronic interaction may indirectly modified the observable gross PECD, as suggested by this work, may prove to be invaluable.

## Acknowledgments

The authors thank the SOLEIL staff for the smooth operation of the facility under proposals n° 20090335, 20100268 and technical support of Jean-François Gil in the DESIRS beamline is warmly acknowledged. The research leading to these results has received funding from the European Community's Seventh Framework Program (FP7/2007-2013) ELISA under grant agreement n.°226716, and the Horizon 2020 Marie Skłodowska-Curie Innovative Training Network (H2020-MSCA-ITN-2015) ASPIRE. The authors would like to acknowledge the use of the EPSRC UK National Service for Computational Chemistry Software (NSCCS) at Imperial College London under project codes CHEM636, CHEM720, CHEM782.

## References

- [1] I. Powis, in *Advances in Chemical Physics*, Vol. 138 (Ed.: J. C. Light), Wiley, New York, **2008**, pp. 267.
- [2] L. Nahon, G. A. Garcia, I. Powis, *J. Electron Spectrosc. Relat. Phenom.* **2015**, *204*, 322.
- [3] E. D. Poliakoff, R. R. Lucchese, *Phys. Scr.* **2006**, *74*, C71.
- [4] J. A. Lopez-Dominguez, D. Hardy, A. Das, E. D. Poliakoff, A. Aguilar, R. R. Lucchese, *J. Electron Spectrosc. Relat. Phenom.* **2012**, *185*, 211.
- [5] A. Das, E. D. Poliakoff, R. R. Lucchese, J. D. Bozek, *J. Chem. Phys.* **2009**, *130*, art. no. 044302.
- [6] W. Domcke, *Phys. Scr.* **1979**, *19*, 11.
- [7] J. Adachi, K. Hosaka, S. Furuya, K. Soejima, M. Takahashi, A. Yagishita, S. K. Semenov, N. A. Cherepkov, *Phys. Rev. Lett.* **2003**, *91*, art. no. 163001.
- [8] D. A. Mistrov, A. De Fanis, M. Kitajima, M. Hoshino, H. Shindo, T. Tanaka, Y. Tamenori, H. Tanaka, A. A. Pavlychev, K. Ueda, *Phys. Rev. A* **2003**, *68*, art. no. 022508.
- [9] N. A. Cherepkov, S. K. Semenov, *Int. J. Quantum Chem.* **2007**, *107*, 2889.
- [10] M. Hoshino, R. Montuoro, R. R. Lucchese, A. De Fanis, U. Hergenhahn, G. Prumper, T. Tanaka, H. Tanaka, K. Ueda, *J. Phys. B-At. Mol. Opt. Phys.* **2008**, *41*.
- [11] E. Plesiat, P. Decleva, F. Martin, *J. Phys. B-At. Mol. Opt. Phys.* **2012**, *45*, 194008.
- [12] R. R. Lucchese, J. Soderstrom, T. Tanaka, M. Hoshino, M. Kitajima, H. Tanaka, A. De Fanis, J. E. Rubensson, K. Ueda, *Phys. Rev. A* **2007**, *76*, 012506.
- [13] M. Hoshino, K. Nakagawa, T. Tanaka, M. Kitajima, H. Tanaka, A. De Fanis, K. Wang, B. Zimmermann, V. McKoy, K. Ueda, *J. Phys. B-At. Mol. Opt. Phys.* **2006**, *39*, 3047.
- [14] E. Plesiat, P. Decleva, F. Martin, *Phys. Rev. A* **2013**, *88*, 063409.
- [15] H. Xu, U. Jacovella, B. Ruscic, S. T. Pratt, R. R. Lucchese, *J. Chem. Phys.* **2012**, *136*, 154303.
- [16] T. Jahnke, L. Foucar, J. Titze, R. Wallauer, T. Osipov, E. P. Benis, A. Alnaser, O. Jagutzki, W. Arnold, S. K. Semenov, N. A. Cherepkov, L. P. H. Schmidt, A. Czasch, A. Staudte, M. Schoffler, C. L. Cocke, M. H. Prior, H. Schmidt-Bocking, R. Dorner, *Phys. Rev. Lett.* **2004**, *93*, art. no. 083002.
- [17] I. Powis, *Phys. Rev. A* **2011**, *84*, 013402.
- [18] G. Contini, N. Zema, S. Turchini, D. Catone, T. Prospero, V. Carravetta, P. Bolognesi, L. Avaldi, V. Feyer, *J. Chem. Phys.* **2007**, *127*, 124310.
- [19] G. A. Garcia, L. Nahon, S. Daly, I. Powis, *Nat. Commun.* **2013**, *4*, 2132.
- [20] C. Lux, M. Wollenhaupt, T. Bolze, Q. Q. Liang, J. Kohler, C. Sarpe, T. Baumert, *Angew. Chem.-Int. Edit.* **2012**, *51*, 5001.
- [21] C. S. Lehmann, N. B. Ram, I. Powis, M. H. M. Janssen, *J. Chem. Phys.* **2013**, *139*, 234307.
- [22] A. Ferré, C. Handschin, M. Dumergue, F. Burgy, A. Comby, D. Descamps, B. Fabre, G. A. Garcia, R. Géneaux, L. Merceron, E. Mével, L. Nahon, S. Petit, B. Pons, D. Staedter, S. Weber, T. Ruchon, V. Blanchet, Y. Mairesse, *Nat. Photon.* **2015**, *9*, 93.
- [23] M. H. M. Janssen, I. Powis, *Phys. Chem. Chem. Phys.* **2014**, *16*, 856.

- [24] M. M. Rafiee Fanood, N. B. Ram, C. S. Lehmann, I. Powis, M. H. M. Janssen, *Nat. Commun.* **2015**, *6*, 7511.
- [25] A. Kastner, C. Lux, T. Ring, S. Zullighoven, C. Sarpe, A. Senftleben, T. Baumert, *ChemPhysChem* **2016**, *17*, 1119.
- [26] M. M. Rafiee Fanood, M. H. M. Janssen, I. Powis, *Phys. Chem. Chem. Phys.* **2015**, *17*, 8614.
- [27] A. Hong, C. M. Choi, H. J. Eun, C. Jeong, J. Heo, N. J. Kim, *Angew. Chem.-Int. Edit.* **2014**, *53*, 7805.
- [28] M. Stener, G. Fronzoni, D. Di Tommaso, P. Decleva, *J. Chem. Phys.* **2004**, *120*, 3284.
- [29] S. Turchini, N. Zema, G. Contini, G. Alberti, M. Alagia, S. Stranges, G. Fronzoni, M. Stener, P. Decleva, T. Prospero, *Phys. Rev. A* **2004**, *70*, art. no.014502.
- [30] S. Stranges, S. Turchini, M. Alagia, G. Alberti, G. Contini, P. Decleva, G. Fronzoni, M. Stener, N. Zema, T. Prospero, *J. Chem. Phys.* **2005**, *122*, 244303.
- [31] G. A. Garcia, H. Dossmann, L. Nahon, S. Daly, I. Powis, *Phys. Chem. Chem. Phys.* **2014**, *16*, 16214.
- [32] M. M. Rafiee Fanood, I. Powis, M. H. M. Janssen, *J. Phys. Chem. A* **2014**, *118*, 11541.
- [33] I. Powis, *J. Chem. Phys.* **2014**, *140*, 111103.
- [34] L. Nahon, N. d. Oliveira, G. Garcia, J. F. Gil, B. Pilette, O. Marcouille, B. Lagarde, F. Polack, *J. Synchrotron Rad.* **2012**, *19*, 508.
- [35] B. Mercier, M. Compin, C. Prevost, G. Bellec, R. Thissen, O. Dutuit, L. Nahon, *J. Vac. Sci. Tech. A* **2000**, *18*, 2533.
- [36] L. Nahon, C. Alcaraz, *Appl. Optics* **2004**, *43*, 1024.
- [37] G. A. Garcia, H. Soldi-Lose, L. Nahon, *Rev. Sci. Instrum.* **2009**, *80*, Art. no. 023102.
- [38] J. C. Pouilly, J. P. Schermann, N. Nieuwjaer, F. Lecomte, G. Gregoire, C. Desfrancois, G. A. Garcia, L. Nahon, D. Nandi, L. Poisson, M. Hochlaf, *Phys. Chem. Chem. Phys.* **2010**, *12*, 3566.
- [39] L. Nahon, G. A. Garcia, C. J. Harding, E. A. Mikajlo, I. Powis, *J. Chem. Phys.* **2006**, *125*, 114309.
- [40] G. A. Garcia, L. Nahon, I. Powis, *Rev. Sci. Instrum.* **2004**, *75*, 4989.
- [41] M. J. Frisch, G. W. Trucks, H. B. Schlegel, G. E. Scuseria, M. A. Robb, J. R. Cheeseman, G. Scalmani, V. Barone, B. Mennucci, G. A. Petersson, H. Nakatsuji, M. Caricato, X. Li, H. P. Hratchian, A. F. Izmaylov, J. Bloino, G. Zheng, J. L. Sonnenberg, M. Hada, M. Ehara, K. Toyota, R. Fukuda, J. Hasegawa, M. Ishida, T. Nakajima, Y. Honda, O. Kitao, H. Nakai, T. Vreven, J. J. A. Montgomery, J. E. Peralta, F. Ogliaro, M. Bearpark, J. J. Heyd, E. Brothers, K. N. Kudin, V. N. Staroverov, T. Keith, R. Kobayashi, J. Normand, K. Raghavachari, A. Rendell, J. C. Burant, S. S. Iyengar, J. Tomasi, M. Cossi, N. Rega, J. M. Millam, M. Klene, J. E. Knox, J. B. Cross, V. Bakken, C. Adamo, J. Jaramillo, R. Gomperts, R. E. Stratmann, O. Yazyev, A. J. Austin, R. Cammi, C. Pomelli, J. W. Ochterski, R. L. Martin, K. Morokuma, V. G. Zakrzewski, G. A. Voth, P. Salvador, J. J. Dannenberg, S. Dapprich, A. D. Daniels, O. Farkas, J. B. Foresman, J. V. Ortiz, J. Cioslowski, D. J. Fox, D.01 ed., Gaussian Inc., Wallingford, CT, **2013**.
- [42] J. P. Merrick, D. Moran, L. Radom, *J. Phys. Chem. A* **2007**, *111*, 11683.
- [43] K. K. Irikura, R. D. Johnson, R. N. Kacker, *J. Phys. Chem. A* **2005**, *109*, 8430.
- [44] I. Pugliesi, K. Muller-Dethlefs, *J. Phys. Chem. A* **2006**, *110*, 4657.
- [45] I. Powis, *J. Chem. Phys.* **2000**, *112*, 301.
- [46] M. Stener, D. D. Tommaso, G. Fronzoni, P. Decleva, I. Powis, *J. Chem. Phys.* **2006**, *124*, 024326.
- [47] I. Powis, C. J. Harding, G. A. Garcia, L. Nahon, *ChemPhysChem* **2008**, *9*, 475.
- [48] L. Nahon, L. Nag, G. A. Garcia, I. Myrgorodska, U. Meierhenrich, S. Beaulieu, V. Wanie, V. Blanchet, R. Géneaux, I. Powis, *Phys. Chem. Chem. Phys.* **2016**, *18*, 12696.
- [49] G. A. Garcia, L. Nahon, C. J. Harding, I. Powis, *Phys. Chem. Chem. Phys.* **2008**, *10*, 1628.

## Figure Captions

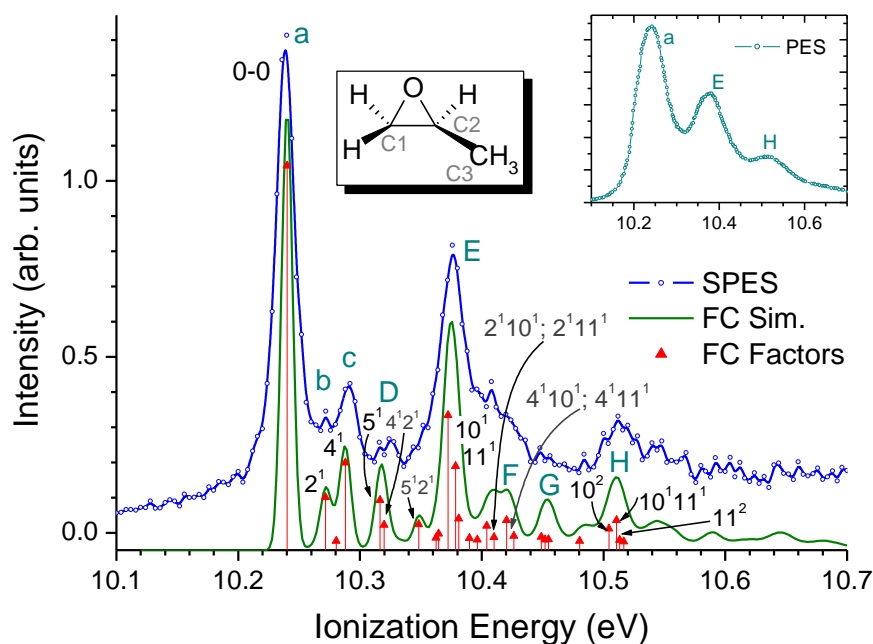


Figure 1 Slow Photoelectron Spectrum (SPES) of S-methyloxirane HOMO<sup>-1</sup> ionization (estimated resolution  $\leq 10$  meV) and a Franck-Condon simulation using B3LYP/cc-pVTZ harmonic analysis of the vibrational structure, with frequencies scaled by 0.97. The stick spectrum excludes the very many less intense transitions for clarity and only assignments relevant for discussion in the text are explicitly indicated. For convenience the peaks are also labelled a – H, where upper case designates the peak as a composite of individual transitions. The inset (top right) shows a moderate resolution PES with the joint progression (a-E-H) in vibrational modes  $\nu_{10}$ ,  $\nu_{11}$  prominent.

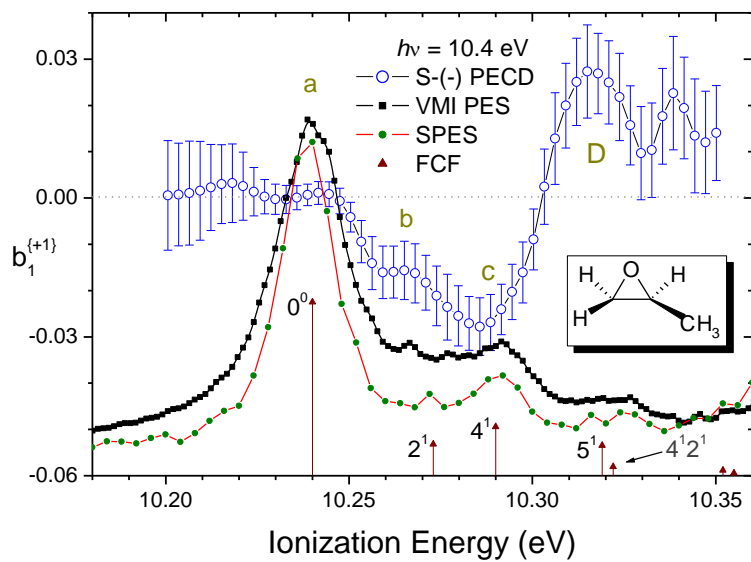


Figure 2 S-Methyl oxirane HOMO band VMI PES and PECD recorded at  $h\nu=10.4$  eV (re-analyzed data from Ref[[19]]). Also included for comparison are the SPES and calculated vibrational transition energies from Fig. 1. These data are drawn on a common energy scale, the photoelectron spectra have arbitrary intensity scales.

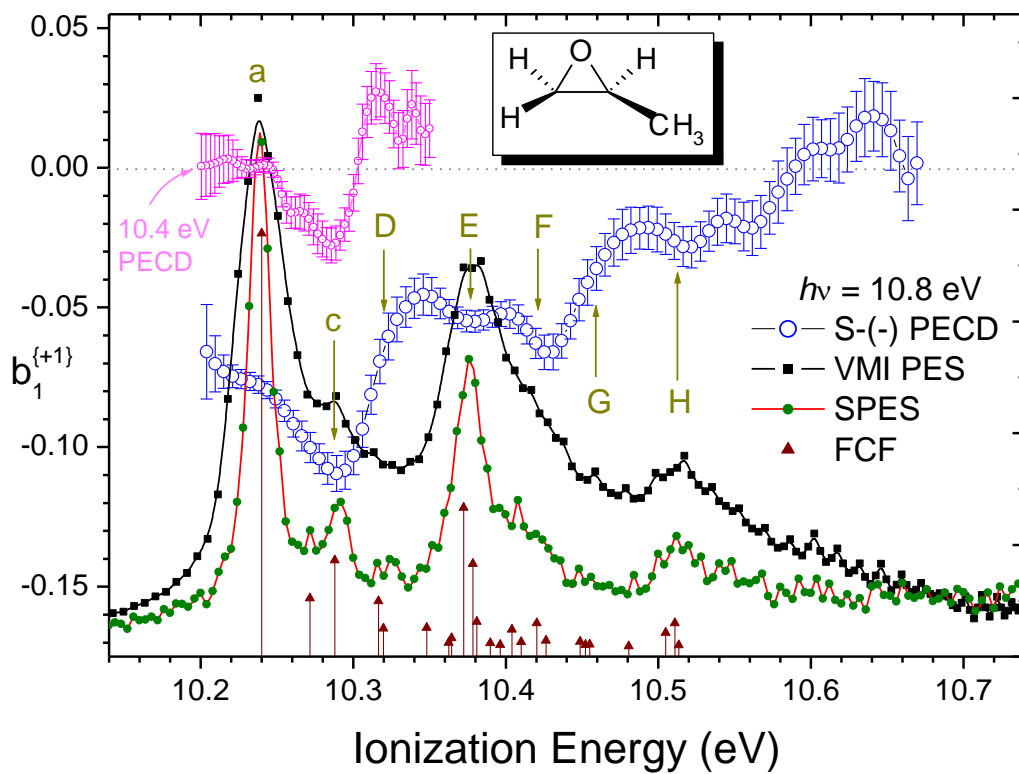


Figure 3 S-Methyl oxirane VMI PES and PECD recorded at  $h\nu = 10.8$  eV. The SPES and calculated vibrational transitions from Fig. 1 are shown on a common energy scale, with the spectra having arbitrary intensity. Also included to facilitate comparison are the  $h\nu = 10.4$  eV PECD data from Fig. 2.

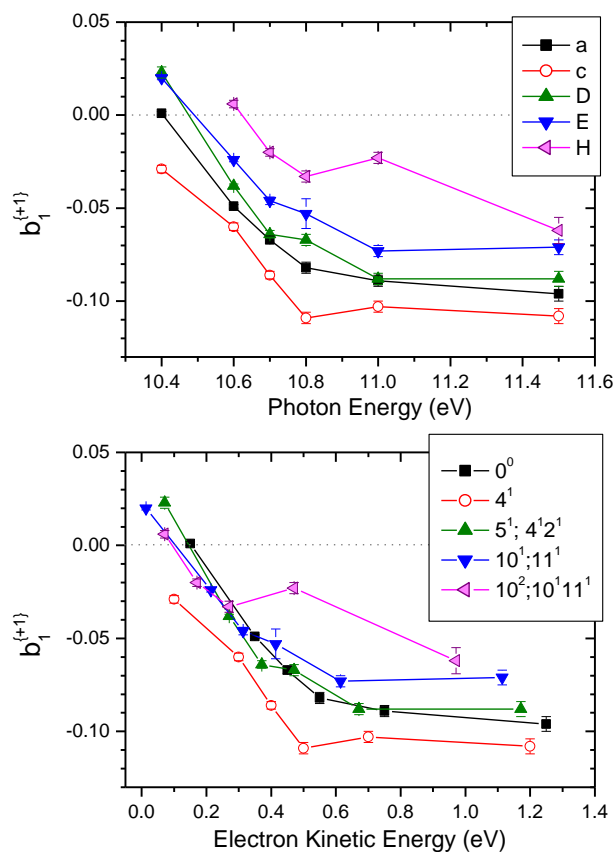


Fig. 4 S-Methyloxirane vibrationally resolved HOMO PECD  $b_1^{\{+1\}}$  parameter versus (top) photon and (bottom) electron kinetic energies. The legend keys show the shorthand peak labels (a—H), or alternatively the vibrational transition assignment, both as they appear in Fig. 1. The single  $h\nu=11$  eV peak H appears to be anomalous.

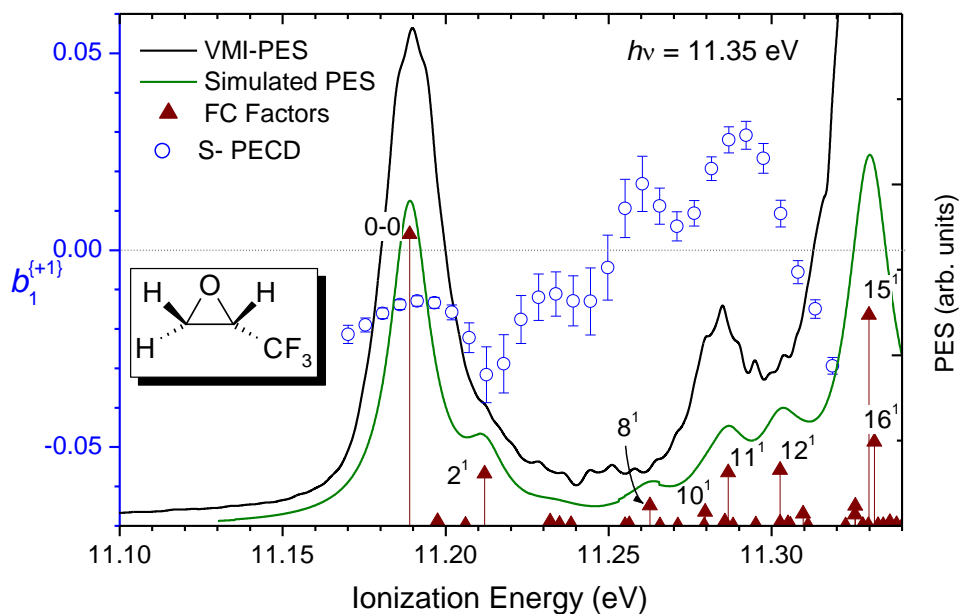


Fig 5. S-Trifluoromethyl oxirane HOMO PECD and PES recorded at 11.35 eV photon energy plotted on a common energy scale. A Franck-Condon simulation using MP2/6-311++G(d) harmonic analysis of the vibrational structure, with frequencies scaled by 0.95 is added for comparison. Only the most intense excitations are shown as individual transitions in the stick spectrum, but the full set of calculated transitions have been convolved with a FWHM $\approx$ 20 meV width function to generate the simulated profile.

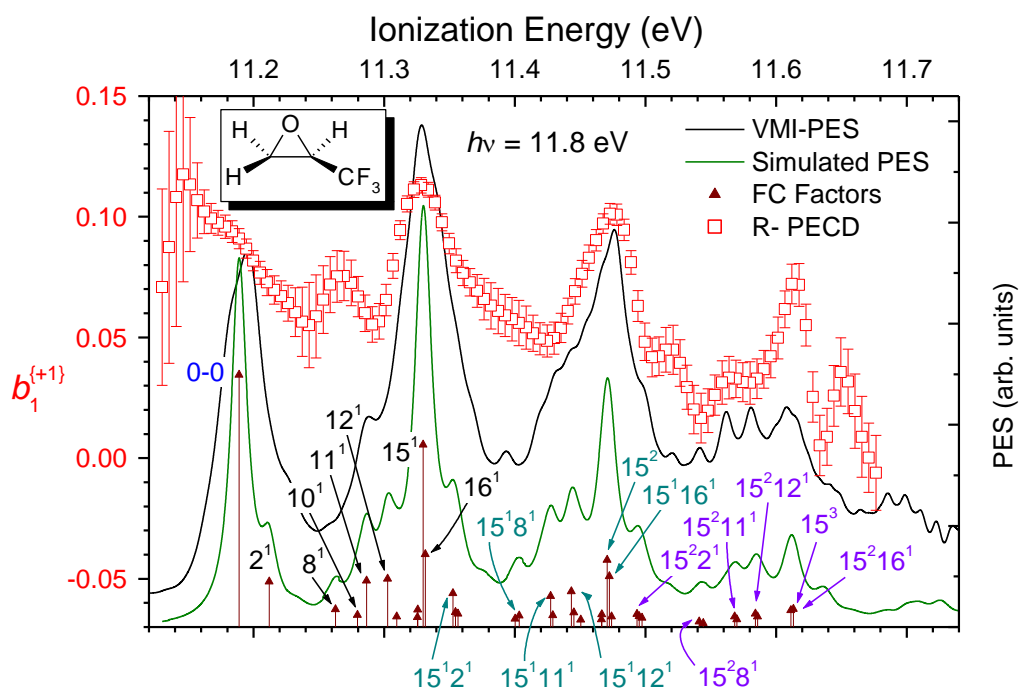


Fig 6 R-Trifluoromethyl oxirane PECD and PES recorded at 11.8 eV photon energy. Other details as Fig. 5.

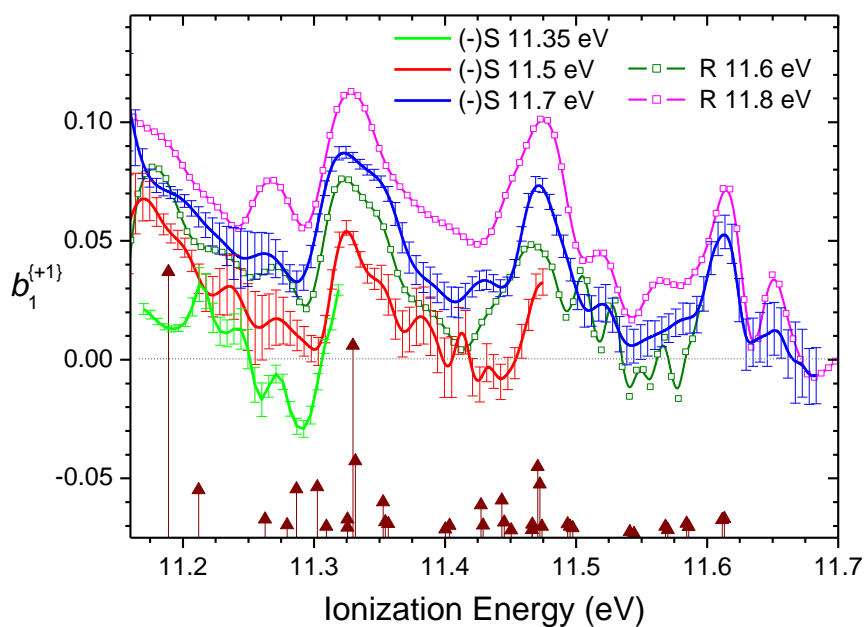


Fig 7 Trifluoromethyl oxirane experimental PECD recorded at indicated photon energies overplotted on a common ionization energy scale. Following theoretical expectation that  $-b_1(S) = b_1(R)$  the S- enantiomer data have been negated before plotting, to facilitate visual comparison with R- enantiomer. For clarity, error bars are only plotted for the S-enantiomer data, but the R-enantiomer error bars are comparable in size. The stick spectrum indicates scaled MP2/6-311++G(d) transition energies and FC factors (as Fig. 5).

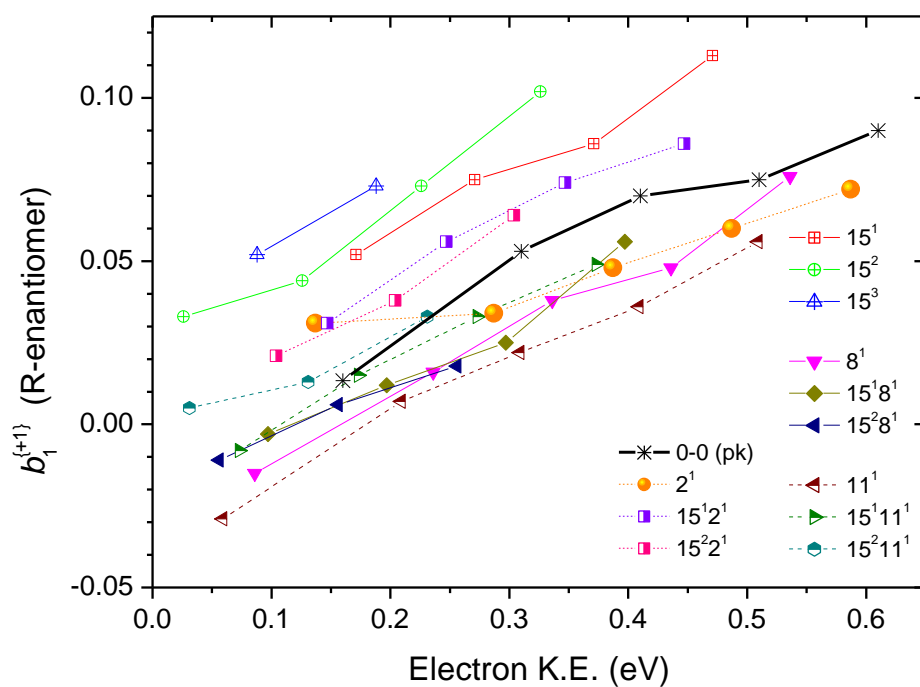


Fig 8 Trifluoromethyloxirane vibration resolved PECD, derived from Fig. 7, as a function of electron kinetic energy. Data points measured with the S-enantiomer are again negated before plotting to facilitate visual comparison. The labelled vibrational assignments are nominal, showing the dominant contribution to an observable peak as identified by the Franck-Condon PES simulation.

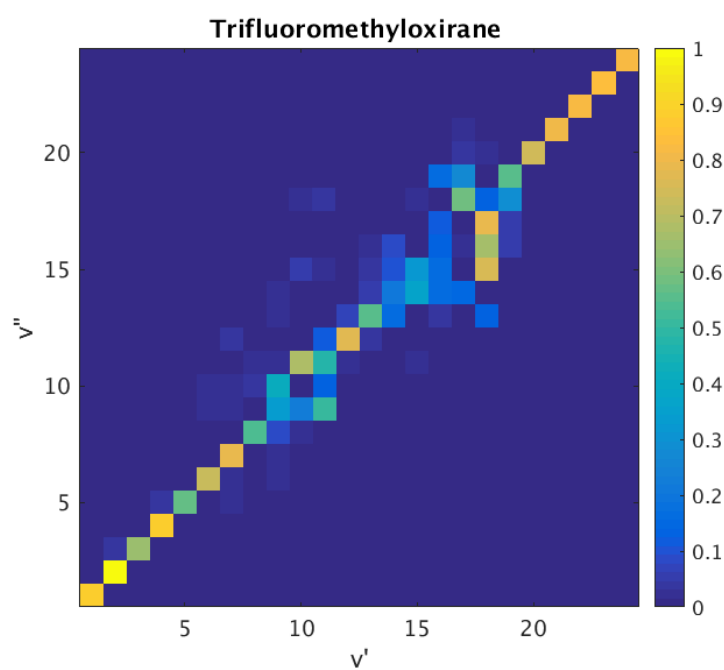
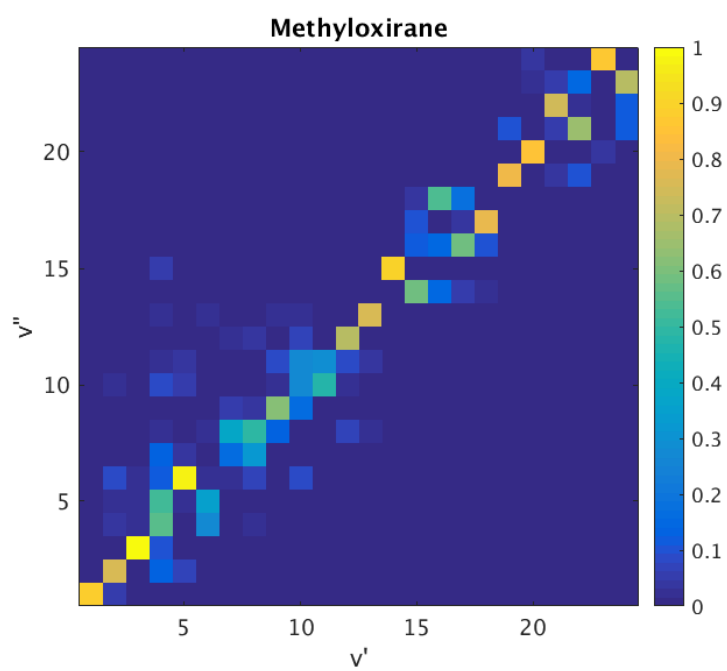


Fig 9 Duschinsky rotation matrices visualised for methyloxirane and trifluoromethyloxirane HOMO<sup>-1</sup> photoionizations.

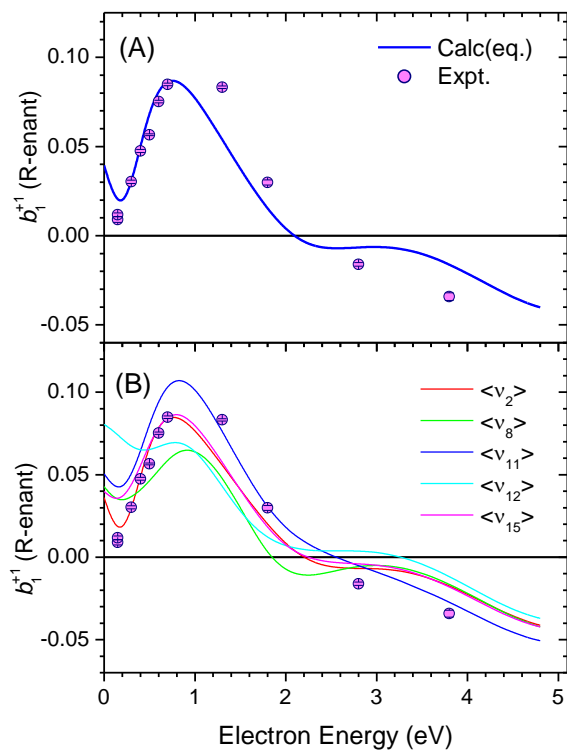


Fig 10. HOMO band PECD Experimental intensity weighted average  $b_1$  values compared against: (A) single fixed equilibrium geometry calculations (Ref. [[31]]); (B) zero point motion averaged calculations for single indicated vibrational modes. The experimental values combine measurements made with both R- and S- enantiomers, negating the latter before plotting.

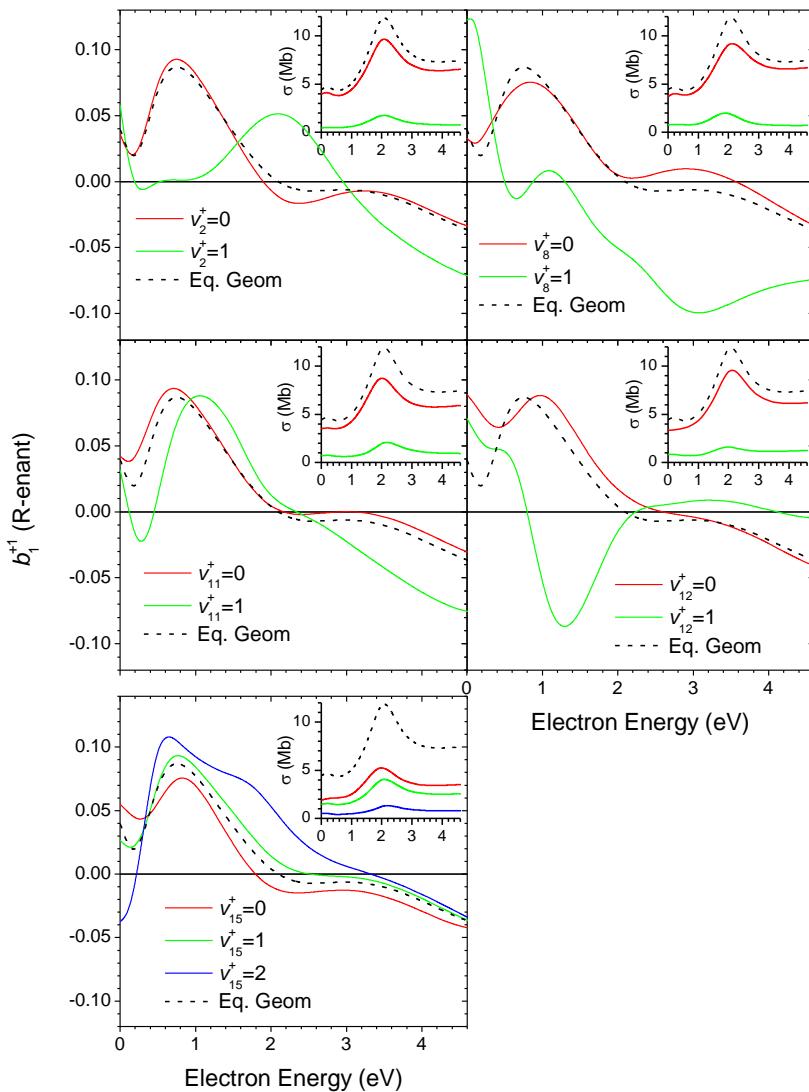


Fig 11. Vibrational resolved PECD calculations for  $v=0, 1$  levels of modes 2,8,11,12, and 15 of R-trifluoromethyloxirane. Each panel includes an inset showing the photoionization cross-sections obtained from the same calculation. For the  $v_{15}$  mode the calculated cross-sections for excited levels do not drop-off so rapidly (as also seen experimentally) and so the two-quantum excitation  $v=2$  is also included. All panels include, as reference, the fixed geometry calculation performed at the equilibrium position.

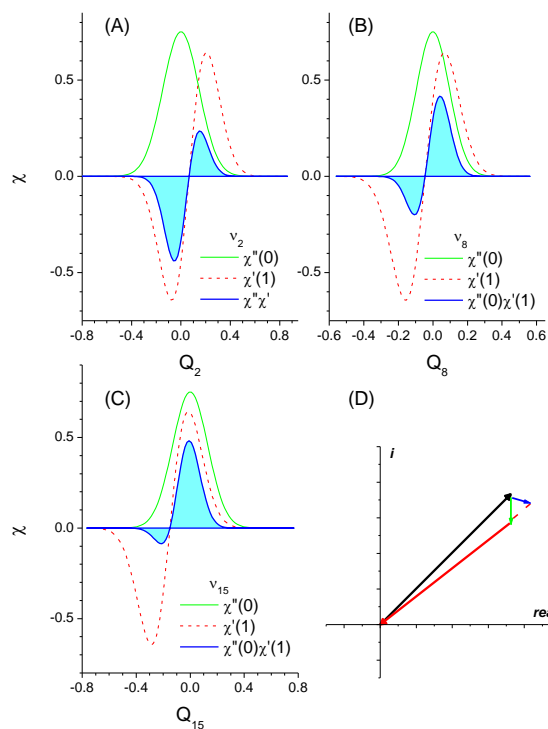
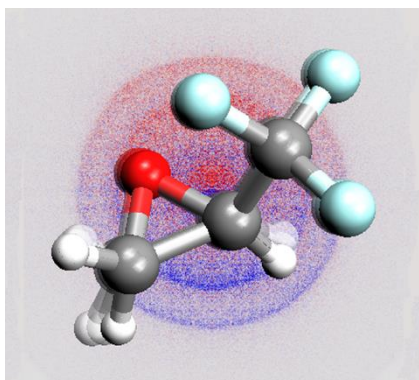


Fig. 12 Neutral  $v=0$ , and ion  $v=1$ , vibrational wavefunctions,  $\chi$ , for selected vibrational modes of trifluoromethyloxirane, and their product  $\chi''\chi'$ . Panels (a) and (b) show, respectively, the weak modes  $v_2$  and  $v_8$  with small geometry displacement; (c) shows the strong  $v_{15}$  mode having a greater relative displacement between ion and neutral potentials. Panel (d) shows schematically the difference (subtraction) between two vectors (red and black) of approximately comparable magnitude/phase in the complex plane. The phase angle of the resultant (green or blue arrows) changes greatly with relatively much smaller changes in, here, the magnitude of the red vector (see text for discussion).

## TOC



**An emerging direction for chiral research?** Photoionization of randomly oriented methyl- and trifluoromethyl-oxirane enantiomers by circularly polarized light emits photoelectrons in preferred directions. This chiral asymmetry is observed using velocity map imaging photoelectron circular dichroism (background example). New studies demonstrate that when weak vibrational modes are excited in the ion, the angular distributions are radically modified, and even reversed.